PAPER

The role of positive and negative pressure on cavitation nucleation in nanodroplet-mediated histotripsy

View the article online for updates and enhancements.

The Role of Positive and Negative Pressure on Cavitation Nucleation in Nanodroplet-Mediated Histotripsy

Eli Vlaisavljevich[1], Omer Aydin[1], Kuang-Wei Lin[1], Yasemin Yuksel Durmaz[2], Brian Fowlkes[1,3], Mohamed ElSayed[1,4*], Zhen Xu[1,5*]

1 - Department of Biomedical Engineering, University of Michigan, Ann Arbor, MI

2- Department of Biomedical Engineering, Schools of Engineering and Natural Science, Istanbul Medipol University, Istanbul, Turkey

3 - Department of Radiology, University of Michigan, Ann Arbor, MI

4 - Macromolecular Science and Engineering Program, University of Michigan, Ann Arbor, MI

5 - Department of Pediatrics and Communicable Diseases, Division of Pediatric Cardiology, University of Michigan, Ann Arbor, MI

*Corresponding Author:
Mohamed E.H. ElSayed, Ph.D.
University of Michigan
Department of Biomedical Engineering
1101 Beal Avenue
Lurie Biomedical Engineering Building
Room 2150
Ann Arbor, MI 48109, USA
Phone: + 1 (734) 615-9404
Fax: + 1 (734) 647-4834
E-mail: melsayed@umich.edu
Web: www.bme.umich.edu/centlab.php

*Corresponding Author:
Zhen Xu, Ph.D.
University of Michigan
Department of Biomedical Engineering
2107 Carl A. Gerstacker Building
2200 Bonisteel Boulevard
Ann Arbor, MI 48109, USA
Phone: + 1 (734) 647-4961
Fax: + 1 (734) 939-1905
E-mail: zhenx@umich.edu
Web:www.bme.umich.edu/labs/xulab/

Abstract

Nanodroplet-mediated histotripsy (NMH) is an ultrasound ablation technique combining histotripsy with acoustically sensitive perfluorocarbon (PFC) nanodroplets that can be selectively delivered to tumor cells for targeted tumor ablation. NMH takes advantage of the significantly reduced cavitation threshold of the nanodroplets, allowing for cavitation to be selectively generated only in regions containing nanodroplets. Understanding the physical mechanisms underlying the nanodroplet cavitation process is essential to the development of NMH. In this study, we hypothesize that cavitation nucleation is caused by the negative pressure (p-) exposed to the PFC, and the NMH cavitation threshold is therefore determined by the incident p- of the single-cycle pulses commonly used in NMH. This paper reports the first study that separately investigates the effects of negative and positive pressure on the NMH cavitation threshold using near half-cycle ultrasound pulses with dominant negative (negative-polarity pulses) or positive (positive-polarity pulses) pressure phases. Tissue phantoms containing perfluorohexane (PFH) nanodroplets were exposed to negative-polarity and positive-polarity pulses generated by a frequency compounding transducer recently developed in our lab, and the probability of generating cavitation was measured as a function of peak negative (p-) and peak positive (p+) pressure. The results showed close agreement in the p- cavitation threshold for PFH phantoms exposed to negative-polarity (11.4±0.1 MPa) and positive-polarity (11.7±0.2 MPa) pulses. The p+ at the cavitation threshold, in contrast, was measured to be significantly different for the negative-polarity (4.0±0.1 MPa) and positive-polarity (42.6±0.2 MPa) pulses. In the final part of this study, the experimental results were compared to the cavitation threshold predicted by classical nucleation theory (CNT), with results showing close agreement between simulations and experiments. Overall, the results support our hypothesis and provide significant insight into the physical mechanisms underlying NMH.

**Keywords**: Nanodroplet, histotripsy, ultrasound, nucleation, cavitation, acoustic droplet vaporization

1 **Introduction**

2   Histotripsy is a noninvasive tissue ablation method that controllably fractionates soft tissue

3 through cavitation generated by high pressure, short duration ultrasound pulses (Parsons *et al.*,

4 2006a; Roberts *et al.*, 2006; Xu *et al.*, 2005). Histotripsy is currently being studied for many clinical

5 applications where non-invasive tissue removal is desired including benign prostatic hyperplasia

6 (Hempel *et al.*, 2011), deep vein thrombosis (Maxwell *et al.*, 2011), congenital heart disease

7 (Owens *et al.*, 2011; Xu *et al.*, 2010), fetal interventions (Kim *et al.*, 2011; Kim *et al.*, 2013), and

8 cancer (Styn *et al.*, 2010; Vlaisavljevich *et al.*, 2013b). Although histotripsy has shown promise for

9 many clinical applications including tumor ablation, this approach is limited to applications in

10 which the target tissue can be identified and imaged prior to treatment, which is often not feasible in

11 cancer patients with many small tumor nodules and micro-metastases. Histotripsy also requires very

12 high pressure ($p->20MPa$), which may not be achievable in some target tissues with limited acoustic

13 access. Due to these limitations, our group has recently developed a targeted ablation approach

14 combing polymer encapsulated nanodroplets with histotripsy (Vlaisavljevich *et al.*, 2013a; Yuksel

15 Durmaz *et al.*, 2014). Nanodroplet-mediated histotripsy (NMH) takes advantage of the significantly

16 reduced cavitation threshold of the nanodroplets, allowing for cavitation to be selectively generated

17 only in regions containing nanodroplets (Vlaisavljevich *et al.*, 2013a). By synthesizing nanodroplets

18 in a size range (~100-400 nm) in which they can diffuse through the leaky tumor vasculature and

19 preferentially accumulate in the tumor, NMH has the potential for selective ablation of tumors

20 (Vlaisavljevich *et al.*, 2013a; Yuksel Durmaz *et al.*, 2014). Previous work has demonstrated that

21 NMH can be used to create well-defined ablation similar to histotripsy but at significantly lower

22 pressure and has the potential to be used for simultaneous multi-focal ablation (Vlaisavljevich *et al.*,

23 2013a).

1   Understanding the physical mechanisms underlying the NMH cavitation process is essential

2   for the development of NMH therapy. Previous studies on acoustic droplet vaporization (ADV)

3   have shown that the ADV vaporization thresholds do not appear to follow the trends predicted by

4   classical nucleation theory (CNT), which predicts that cavitation will be nucleated inside the

5   droplets directly from the applied negative pressure (p-) (Arvengas *et al.*, 2011; Caupin and Herbert,

6   2006; Fisher, 1948; Herbert *et al.*, 2006; Kripfgans *et al.*, 2004; Kripfgans *et al.*, 2000; Schad and

7   Hynynen, 2010; Sheeran and Dayton, 2012; Williams *et al.*, 2013). These studies have led to the

8   hypothesis that nanodroplet nucleation in ADV is caused by a different mechanism than what is

9   predicted by CNT, such as droplet deformation, hydrodynamic cavitation, or acoustic heating

10   (Kripfgans *et al.*, 2004; Kripfgans *et al.*, 2000; Sheeran and Dayton, 2012). However, these ADV

11   studies used larger droplets, higher frequency ranges, and pulses with more acoustic cycles than

12   those used in NMH therapy (Kripfgans *et al.*, 2004; Kripfgans *et al.*, 2000; Schad and Hynynen,

13   2010; Sheeran and Dayton, 2012; Vlaisavljevich *et al.*, 2015a; Vlaisavljevich *et al.*, 2015b;

14   Vlaisavljevich *et al.*, 2013a; Williams *et al.*, 2013; Yuksel Durmaz *et al.*, 2014). Furthermore,

15   recent work reveals that the decrease in the ADV threshold at higher frequencies is due to

16   superharmonic focusing, which significantly increases the amplitude of the p- inside the droplet and

17   is enhanced at higher frequencies and in larger droplets (Li *et al.*, 2014; Shpak *et al.*, 2014).

18   Therefore, it is possible that ADV nucleation does in fact follow the predictions of CNT, once the

19   effects of pressure focusing are accounted for.

20   In NMH, cavitation bubbles are generated from nanodroplets <600 nm in diameter using

21   single-cycle ultrasound pulses at frequencies in the hundreds of kHz to low MHz range, resulting in

22   cavitation thresholds significantly higher than the vaporization thresholds previously measured for

23   ADV (Kripfgans *et al.*, 2004; Vlaisavljevich *et al.*, 2015a; Vlaisavljevich *et al.*, 2015b;

24   Vlaisavljevich *et al.*, 2013a; Yuksel Durmaz *et al.*, 2014), with the trends appearing the follow the

1   predictions of CNT (Arvengas *et al.*, 2011; Caupin and Herbert, 2006; Fisher, 1948; Herbert *et al.*,

2   2006; Vlaisavljevich *et al.*, 2015c). For example, previous work has demonstrated a significant

3   reduction in the histotripsy cavitation threshold for both perfluoropentane (PFP) and

4   perfluorohexane (PFH) nanodroplets exposed to single cycle histotripsy pulses (Kawabata *et al.*,

5   2010; Maxwell *et al.*, 2013; Vlaisavljevich *et al.*, 2015a; Vlaisavljevich *et al.*, 2015b; Vlaisavljevich

6   *et al.*, 2015c). The NMH cavitation threshold decreases at lower frequencies (Vlaisavljevich *et al.*,

7   2015a; Vlaisavljevich *et al.*, 2015b), in contrast to the increasing ADV threshold with higher

8   frequency observed using micron sized droplets (Kripfgans *et al.*, 2004; Kripfgans *et al.*, 2000;

9   Schad and Hynynen, 2010; Williams *et al.*, 2013). The NMH frequency dependence appears to

10   agree with CNT, which predicts that lower frequency will decrease the cavitation threshold due to

11   the longer duration of the applied $p-$ and the larger focal zone at lower frequencies (Arvengas *et al.*,

12   2011; Caupin and Herbert, 2006; Fisher, 1948; Herbert *et al.*, 2006; Vlaisavljevich *et al.*, 2015a;

13   Vlaisavljevich *et al.*, 2015b; Vlaisavljevich *et al.*, 2015c). Furthermore, a slight increase in the

14   NMH cavitation threshold has been observed for PFH nanodroplets compared to PFP droplets due

15   to the increase in the surface tension and boiling point of PFH, which also agrees with the

16   predictions of CNT (Arvengas *et al.*, 2011; Caupin and Herbert, 2006; Fisher, 1948; Herbert *et al.*,

17   2006; Vlaisavljevich *et al.*, 2015a; Vlaisavljevich *et al.*, 2015b; Vlaisavljevich *et al.*, 2015c).

18   Based on these previous studies, we hypothesize that NMH bubbles are generated after

19   cavitation is nucleated inside the droplets directly from the incident $p-$ (tensile portion of the

20   incident wave), similar to histotripsy bubbles generated without nanodroplets when the negative

21   pressure directly exceeds the intrinsic threshold (Maxwell *et al.*, 2013; Vlaisavljevich *et al.*, 2015c;

22   Lin *et al.*, 2014a). In order to test this hypothesis, in this study we separate the effects of negative

23   and positive pressure on NMH cavitation nucleation using near half-cycle ultrasound pulses with

24   dominant negative (negative-polarity pulses) or positive (positive-polarity pulses) pressure phases.

This paper reports the first study that separately investigates the effects of negative and positive pressure on the NMH cavitation process. The generation of near monopolar pulses was made possible by using a frequency compounding transducer recently developed in our lab, which aligns the positive or negative phases of multiple-frequency components while destructive interference occurs elsewhere in space and time, leading to pulses with a single dominant negative or positive pressure phase (Lin *et al.*, 2014a). Tissue phantoms containing PFH nanodroplets and control phantoms without droplets were exposed to negative-polarity and positive-polarity pulses, and optical imaging was used to measure the NMH cavitation threshold as a function of peak negative (p-) and peak positive ($p+$) pressure. The NMH cavitation threshold definition is similar to the ADV threshold, with the difference being in the type of bubble that is generated from the nanodroplets (i.e. transient cavitation bubble vs. stable ADV bubble). Finally, to help explain the experimental results, CNT was used to theoretically investigate the expected cavitation thresholds for samples with and without PFH nanodroplets, with the CNT results compared to the experimentally observed thresholds. Overall, the results of this study will improve our understanding of the physical mechanisms underlying the NMH cavitation process, which is essential for the development of NMH therapy.

Methods

Nanodroplet Formulation and Characterization

Polymer encapsulated perfluorohexane (PFH, SynQuest Lab, > 98%) nanodroplets were used for this study based on recent work demonstrating that PFH droplets have many benefits for NMH therapy (Vlaisavljevich *et al.*, 2015a). A PEG_{45}-*b*-PAA_{12}-*b*-$P(HDFMA_8$-*co*-$MMA_{20})$ triblock copolymer was synthesized using a combination of atom transfer radical polymerization (ATRP) and "click" coupling chemistry to prepare PFH-loaded nanodroplets following our published

1   method (Yuksel Durmaz *et al.*, 2014). Formulation of PFH-loaded nanodroplets started by

2   dissolving the polymer in tetrahydrofuran (THF) (0.2% w/v) and cooling the solution down to 0°C

3   before adding PFH (2% v/v) while vigorously stirring the reaction mixture. An equal volume of

4   deionized water was added drop-wise to this solution to initiate micelle formation and the mixture

5   was stirred for 1 hour in an ice bath. The micelles solution was transferred to a dialysis bag

6   (MWCO of 1 KDa, Spectrum, Rancho Dominguez, CA) and dialyzed overnight against ice-cold

7   MES buffer solution (pH 5.5) to remove the THF solvent and get a milky solution of non-cross-

8   linked PFH-loaded nanodroplets. The milky nanodroplets solution was transferred to a round

9   bottom flask and mixed with the 2,2`-(ethylenedioxy)-bis(ethylamine) cross-linker to react with the

10   carboxyl groups of the central PAA block in the polymer backbone via NHS/EDC coupling

11   chemistry forming cross-linked nanodroplets with a flexible polymer shell. Shell cross-linked

12   nanodroplets were dialyzed against ice-cold water for 12 hours to remove unreacted cross-linker

13   and reaction byproducts .

14   Concentration and size distribution of the nanodroplets were measured using Nanoparticle

15   Tracking Analysis (NTA). Briefly, the NanoSight™ LM10 (Malvern Instruments, Amesbury, UK),

16   equipped with a temperature-controlled 405 nm laser module, high sensitivity Scientific

17   Complementary Metal–Oxide–Semiconductor (sCMOS) camera (Hamamatsu, Orca, Hamamatsu

18   City, Japan), and a syringe pump was used for the collection of NTA data. Upon diluting the

19   nanodroplet solution to the appropriate particle concentration with deionized (DI) water (Thermo

20   Scientific, GenPure, Waltham, MA, USA), image capture and analysis was carried out using the

21   NTA software (Version 3.0, Build 0066, Malvern Instruments, Amesbury, UK) at $37^{°}$C. The

22   samples were measured by capturing 60s videos (5 videos per each sample). These values were

23   determined in order to collect sufficient data such that the shape of the histogram no longer changed

24   significantly with additional data (i.e. NTA analyzed hundreds or thousands of particles in order to

1 calculate a representative particle size distribution). **Figure 1** is a representative plot showing the

2 size distribution of the PFH nanodroplets. The error bars represent the standard deviation of the

3 repeat measurements of each sample. The mean size and standard deviation values obtained by the

4 NTA software correspond to arithmetic values calculated with the sizes of all particles analyzed for

5 each sample (n=5). Results from all samples demonstrated that the average size of the nanodroplets

6 (NDs) was 233±3.9 nm with 10% of NDs have a diameter ≤ 135.3±2.6 nm, 50% of the NDs have a

7 diameter ≤ 192.7±5.3 nm, 90% of the NDs have a diameter ≤ 373.7±7.2 nm, and >99% of the NDs

8 are ≤ 600 nm.

9

10 *Preparation of Tissue Phantoms*

11   Agarose phantoms were used to provide a well-controlled viscoelastic medium for this

12 study. Tissue phantoms containing 1% agarose w/v were prepared by slowly mixing agarose

13 powder (Agarose Type VII; Sigma-Aldrich, St. Louis, MO, USA) into saline solution (0.9% sodium

14 chloride; Hospira, Lake Forest, Illinois, USA) heated to boiling temperature. The solution was

15 stirred on a hot plate until the gel turned completely transparent and then allowed to boil for ten

16 minutes. After boiling, solutions were allowed to cool and were degassed under a partial vacuum

17 (~20 kPa, absolute) for 30 minutes. After degassing, phantoms containing nanodroplets were

18 prepared by slowly adding the nanodroplets (2.0×10^8 particles/ml) into the agarose solution while

19 stirring. The agarose mixtures were poured into polycarbonate holders and placed in a refrigerator at

20 4°C to allow the solution to solidify, forming tissue phantoms with embedded PFH nanodroplets

21 and without nanodroplets (control). Tissue phantoms containing PFH nanodroplets were assumed to

22 have a nearly uniform distribution of droplets throughout the phantom, which is supported by the

23 observations in previous NMH studies which showed similar cavitation thresholds and bubble

24 activity for treatments applied throughout all regions of these tissue phantoms (Vlaisavljevich *et al.*,

1 2015b; Vlaisavljevich *et al.*, 2013a; Yuksel Durmaz *et al.*, 2014). The attenuation coefficients of the

2 agarose tissue phantoms with and without PFH droplets were measured to be <0.1 dB/cm for the

3 pulses used in this study. These values, along with the short propagation distance through the

4 phantom (<2 cm), suggest that attenuation from the tissue phantoms will have a negligible impact

5 on the reported pressure values which were measured in free field.

6

Histotripsy Pulse Generation

8 Histotripsy pulses with dominant negative (negative-polarity pulse) and positive (positive-

9 polarity pulse) pressure phases were generated used a frequency compounding transducer, adapted

10 from a previous study (Lin *et al.*, 2014a). The frequency-compounding transducer was composed of

11 12 elements (20 mm in diameter) with various resonant frequencies: 500 kHz (three elements), 1

12 MHz (two elements), 1.5 MHz (two elements), 2 MHz (two elements), and 3 MHz (three elements)

13 (Lin *et al.*, 2014a). The elements had a common geometric focus at 40 mm and were populated in a

14 scaffold in a specific order to ensure that adjacent elements did not have the same frequency. This

15 was done to reduce nonlinear propagation effects that occur when acoustic waves of the same

16 frequency propagate closely in space and interfere constructively. Additionally, the frequency-

17 compounding transducer has two diametrically opposed optical windows to allow for optical

18 imaging at the geometric focus. The design of the frequency compounding transducer has been

19 described in detail in a previous study (Lin *et al.*, 2014a).

20 A custom high voltage pulser with 12 parallel channels was used to drive the frequency-

21 compounding transducer. The pulser was connected to a field-programmable gated array (FPGA)

22 development board (Altera DE1, Terasic Technology, Dover, DE, USA) specifically programmed

23 for frequency compounding pulse generation. This setup allowed each element to individually

24 output short pulses with only one large negative or positive pressure phase. The generation of

1 negative-polarity pulses was achieved by adjusting the arrival times of individual frequency

2 components to allow their principal negative phase peaks to arrive at the focus of the transducer

3 concurrently (**Fig.2A**). In this situation, destructive interference occurs elsewhere in space and time,

4 leading to a diminution of the peak positive pressure of the combined ultrasound pulse (**Fig.2A**).

5 For the generation of positive-polarity pulses, the driver pulses for the individual elements were

6 inverted, resulting in ultrasound pulses with a single principal positive phase from each element.

7 The arrival times of individual frequency components were then adjusted to allow their principal

8 positive phase peaks to arrive at the focus concurrently (**Fig.2B**).

9 A fiber-optic probe hydrophone (FOPH) built in-house (Parsons *et al.*, 2006b) was used to

10 calibrate and measure the acoustic output of the frequency-compounding transducer, with example

11 waveforms shown in **Figure 2**. For threshold experiments, the probability of cavitation (measured

12 by optical imaging) was plotted as a function of both the peak negative (p-) and peak positive (p+)

13 pressure. In order to determine the peak pressure values for the negative and positive polarity

14 pulses, 2D spatial pressure fields were directly measured using the FOPH in order to identify the

15 locations corresponding to the p- and p+ in the focal region. The ratio of p- to p+ measured for the

16 negative-polarity pulses in this location was between 2.9-3.7 for the pressure ranges used in this

17 study. For the positive-polarity pulses, the 2D spatial pressure fields measured by the FOPH

18 demonstrated the location of the p- in the focal region occurred ~0.5 mm away from the geometric

19 focus, while the location of the p+ remained near the geometric focus (**Fig.3**). This effect is due to

20 the temporal alignment of the principle peak positive peaks of the individual frequency components

21 at the geometric focus, which resulted in a near monopolar positive pulse at the geometric focus

22 with two low-negative-pressure lobes outside of the focal region. The ratio of p+ to p- for the

23 positive-polarity pulses was measured to be between 3.2-3.9 for the pressure ranges used in this

24 study using the p+ and p- measured at the maximum locations in the field. For the positive polarity

1   pulses, the pressure was directly measured up to the maximum output of the transducer, p-

2   $/p+$=16.3/55.1 MPa. For the negative polarity pulses, the pressure at the focus could only be

3   directly measured up to p-$/p+$=21.5/7.6 MPa due to cavitation at the fiber tip at higher pressures.

4   The pressures above this value were estimated using a linear summation of the pressures measured

5   for individual elements, as outlined in previous studies (Lin *et al.*, 2014a; Maxwell *et al.*, 2013;

6   Vlaisavljevich *et al.*, 2015c; Vlaisavljevich *et al.*, 2015d).

7

8   *Optical Imaging and Image Processing*

9   High speed optical imaging was used to capture images of the focal zone after the

10 propagation of each pulse through the focus. The frequency compounding transducer was placed on

11 the bottom of a tank of degassed water, and a tissue phantom attached to a 3-axis motorized

12 positioning system was lowered into the focus of the transducer (**Fig.4**). A digital, 1.3-megapixel

13 CCD camera (PN: FL3-U3-13Y3M-C, Flea® 3, PointGrey, Richmond, BC, Canada) was positioned

14 perpendicularly to the frequency compounding transducer facing one of the transducer's optical

15 windows (**Fig.4**). A Nikon 4X objective was attached to the camera with extension tubes to magnify

16 the image plane, giving the captured images a resolution of approximately 3.6 µm per pixel. A

17 pulsed white-light LED was placed on the diametrically-opposed optical window of the dual-

18 frequency array transducer, which provided back-lit illumination. The cameras were triggered to

19 record one image after the passage of each pulse at a time point approximately corresponding to the

20 maximum bubble expansion. This time point was determined for the negative-polarity and positive-

21 polarity pulses prior to experiments by changing the delay time on the camera to identify the time

22 corresponding to maximum bubble expansion, as described in previous studies (Vlaisavljevich *et*

23 *al.*, 2015b; Vlaisavljevich *et al.*, 2015c; Vlaisavljevich *et al.*, 2015d). After acquisition,

24 shadowgraph images were converted from grayscale to binary by an intensity threshold determined

1 by the background intensity using image processing software (MATLAB, The Mathworks, Natick,

2 MA, USA), as described in a previous study (Maxwell *et al.*, 2013). Bubbles were indicated as any

3 black regions greater than 5 pixels in diameter. By this criterion, the minimum resolvable bubble

4 radius was 9 μm.

5

6 *NMH Cavitation Threshold*

7   For cavitation threshold experiments, 100 pulses were applied inside each sample at each

8 pressure level at a pulse repetition frequency (PRF) of 0.5 Hz. The PRF was kept low to minimize

9 the possibility that cavitation from one pulse would change the probability of cavitation on a

10 subsequent pulse. In a previous study, it was demonstrated that cavitation during a pulse increased

11 the likelihood of cavitation on a following pulse for PRFs > 1 Hz, but this effect was not observed

12 for PRFs < 1 Hz (Maxwell *et al.*, 2013). In addition to this low PRF, the phantom sample was

13 translated for each pulse by 1 mm transverse to the acoustic propagation direction in a 10×10 grid

14 in order to minimize the effects of cavitation damage to the nanodroplets from altering the

15 probability of cavitation. Using this method, each point in the tissue phantom was exposed to a

16 single pulse at a single pressure amplitude. For each pulse, cavitation was monitored using high

17 speed imaging, and the fraction of total pulses at a given pressure level (out of 100) for which

18 cavitation was detected was determined as the cavitation probability.

19   The probability of observing cavitation followed a sigmoid function, given by

$$P(p) = \frac{1}{2} + erf\left(\frac{p - p_t}{\sqrt{2\sigma^2}}\right) \ (\mathbf{E1})$$

20 where *erf* is the error function, p_t is the pressure at which the probability p_{cav}=0.5, σ is a variable

21 related to the width of the transition between p_{cav}=0 and p_{cav}=1, with $\pm \sigma$ giving the difference in

22 pressure from about p_{cav}=0.15 to p_{cav}=0.85 for the fit (Maxwell *et al.*, 2013). The cavitation

1   threshold for each sample, p_t, is defined as the pressure, p, corresponding to $p_{cav}=0.5$ as calculated

2   by the curve fit. Curve fitting for all data sets was performed using an OriginLab curve fitting

3   program (OriginPro 9.1; OriginLab Corporation, Northampton, MA, USA). The fit curves for all

4   samples were analyzed statistically to determine whether the differences in the values of p_t were

5   significantly different from each other. The standard errors for p_t were estimated by a covariance

6   matrix using the delta method (Hosmer and Lemeshow, 1992). The curves were compared using a

7   two-sample t-test with statistic $t\left(p_{int1} - p_{int2}, \sqrt{SE_1^2 + SE_2^2}\right)$ at a 95% confidence interval. Results

8   were considered statistically significant for p<0.05. Note that the standard error does not include the

9   uncertainty in absolute pressure from the hydrophone measurement, only the uncertainty in the fit,

10   because the values p_t are relative. For each sample, the curves were analyzed as a function of both

11   positive and negative pressure, with the corresponding cavitation threshold values calculated as

12    $p_t(+)$ and $p_t(-)$, respectively. A sample size of 3 tissue phantoms was used for each experimental

13   condition (i.e. phantoms containing PFH nanodroplets or no nanodroplets exposed to negative-

14   polarity or positive-polarity pulses).

15

16   *Classical Nucleation Theory Simulation*

17   A theoretical analysis was performed based on classical nucleation theory (CNT) in order to

18   theoretically investigate the expected cavitation thresholds (Arvengas *et al.*, 2011; Caupin and

19   Herbert, 2006; Herbert *et al.*, 2006; Pettersen *et al.*, 1994). Previous studies using CNT suggest that

20   the cavitation threshold is dependent upon the properties of the media (i.e. temperature, surface

21   energy) as well as the spatial and temporal distribution of the applied $p-$ (Arvengas *et al.*, 2011;

22   Pettersen *et al.*, 1994). In this study, CNT was used to calculate the theoretical cavitation thresholds

23   for samples with and without PFH nanodroplets. The CNT results were then compared to the

24   experimental thresholds measured for the near monopolar pulses used in this study as well as for

1 dual polarity pulses at frequencies ranging from 345 kHz to 3 MHz used in previous studies

2 (Vlaisavljevich *et al.*, 2015c; Vlaisavljevich *et al.*, 2015b). The threshold predicted by CNT, p_{CNT},

3 was calculated as

$$p_{CNT} = \left(\frac{16\pi\alpha^3}{3k_bT*\ln\frac{\Gamma_0 V_f \tau_f}{\ln 2}} \right)^{0.5} \quad \textbf{(E7)}$$

5 where α is the surface energy, k_b is the Boltzmann's constant, T is temperature in Kelvin, Γ_0 is a

6 prefactor, V_f is the focal volume for a given frequency, and τ_f is the time the focal volume is above a

7 given pressure (Arvengas *et al.*, 2011; Caupin and Herbert, 2006; Fisher, 1948; Herbert *et al.*, 2006;

8 Pettersen *et al.*, 1994). Γ_0 was set to $\Gamma_0=10^{33}$ similar to previous work (Pettersen *et al.*, 1994;

9 Vlaisavljevich *et al.*, 2015c). V_f and τ_f were modified for each frequency with τ_f set to one fourth of

10 the acoustic period and V_f representing the volume of fluid exposed to the applied pressure. An

11 effective frequency of 1.8 MHz was used for the frequency compounding transducer, as calculated

12 based on the duration of the applied p- pressure cycle shown in **Figure 2A**. The values of V_{f_water}

13 were calculated from the -6 dB FWHM beam profiles of the transducers assuming an ellipsoidal

14 focus, and were 47.07 mm^3, 7.89 mm^3, 2.30 mm^3, 0.072 mm^3, and 1.04 mm^3 for 345 kHz, 500 kHz,

15 1.5 MHz, 3 MHz, and the frequency compounding transducer (1.8 MHz), respectively. For

16 simulations of the cavitation threshold without droplets, the surface energy of water, α_w, was set to

17 19 mN/m, ~25% of the macroscopic surface tension of water, based on previous work showing this

18 value provides a more reasonable agreement with experimentally observed cavitation thresholds

19 (Arvengas *et al.*, 2011; Herbert *et al.*, 2006; Vlaisavljevich *et al.*, 2015c).

20   To theoretically investigate the cavitation threshold in phantoms containing PFH droplets,

21 the CNT simulation was modified to account for the lower surface energy of PFH, α_{PFH}, which was

22 set to 11.9 mN/m to match the macroscopic surface tension of PFH (Hougham *et al.*, 1999). In

23 addition, the PFH threshold simulation was corrected to account for only the volume of PFH within

14

1   the focal region. The volume of PFH in the focal region, V_{f_PFH}, was calculated by multiplying

2   V_{f_water} by the amount of PFH in a unit volume of water, as calculated from the particle

3   concentration and size distribution data shown in **Figure 1**. The resulting values of V_{f_PFH} were 0.31

4   mm^3, 0.051 mm^3, 0.015 mm^3, 0.00046 mm^3, and 0.0068 mm^3 for 345 kHz, 500 kHz, 1.5 MHz, 3

5   MHz, and the frequency compounding transducer (1.8 MHz), respectively.

6

Results

NMH Cavitation Threshold: Negative-Polarity Pulse

9   In the first set of experiments, the histotripsy cavitation threshold was measured for agarose

10   tissue phantoms with and without PFH nanodroplets exposed to negative-polarity pulses (**Fig.2A**).

11   For both types of phantoms, cavitation bubbles were only observed on the high-speed camera once

12   a certain pressure threshold was exceeded (**Fig.5**), as seen in previous studies (Maxwell *et al.*, 2013;

13   Vlaisavljevich *et al.*, 2015a; Vlaisavljevich *et al.*, 2015b; Vlaisavljevich *et al.*, 2015c). As the

14   pressure was further raised above this threshold value, cavitation was observed in an increasingly

15   larger region of the focal area, forming well-defined histotripsy bubble clouds similar to those

16   observed in previous work using dual-polarity pulses at various frequencies (Maxwell *et al.*, 2013;

17   Vlaisavljevich *et al.*, 2015a; Vlaisavljevich *et al.*, 2015b; Vlaisavljevich *et al.*, 2015c;

18   Vlaisavljevich *et al.*, 2015d). Plotting the probability of cavitation as a function of *p-* demonstrated

19   a significant decrease in $p_t(-)$ for tissue phantoms containing nanodroplets compared to control

20   phantoms (**Fig.6A,B**), with the *p-* threshold measured to be $p_{t\_}(-) = 29.8{\pm}0.3$ MPa, with $\sigma_{mean} = 0.7$

21   MPa for control phantoms without nanodroplets and $p_t(-) = 11.7{\pm}0.2$ MPa, with $\sigma_{mean} = 0.4$ MPa for

22   PFH phantoms. These results closely matched the *p-* thresholds measured in previous studies using

23   single-cycle dual-polarity pulses with center frequencies ranging from 345kHz to 3MHz (**Table 1**).

24   The single-cycle dual-polarity pulses commonly used in histotripsy studies contain both high

1   amplitude positive and negative pressure phases (**Fig.2C**). The p- thresholds for generating

2   cavitation previously measured with the dual-polarity pulse were 24 MPa–27 MPa without

3   nanodroplets and 10 MPa–15 MPa with PFH nanodroplets (**Table 1**) (Vlaisavljevich *et al.*, 2015a;

4   Vlaisavljevich *et al.*, 2015b; Vlaisavljevich *et al.*, 2015c). Plotting the probability of cavitation for

5   the negative-polarity pulses as a function of $p+$ demonstrated a significant decrease in $p_t(+)$ for

6   tissue phantoms containing nanodroplets compared to control phantoms (**Fig.7A,B**), with the $p+$

7   threshold measured to be $p_{t\_}(+) = 9.9\pm0.1$ MPa, with $\sigma_{mean} = 0.2$ MPa for control phantoms and $p_t(+)$

8    $= 4.0\pm0.1$ MPa, with $\sigma_{mean} = 0.2$ MPa for PFH phantoms. The $p+$ threshold results measured for the

9   negative-polarity pulses were significantly different than the $p+$ thresholds measured in previous

10   studies using dual-polarity pulses, which ranged from $p_t(+) = 28.1$ MPa–51.2 MPa and $p_t(+) = 10.2$

11   MPa–15.8 MPa for control and PFH phantoms, respectively (**Table 1**).

12

13   *NMH Cavitation Threshold: Positive-Polarity Pulse*

14   In the second set of experiments, the histotripsy cavitation threshold was measured for tissue

15   phantoms with and without PFH nanodroplets exposed to positive-polarity pulses (**Fig.2B**). For

16   control phantoms without nanodroplets, cavitation bubbles were not consistently observed in the

17   focal region at any of the pressure levels tested (**Fig.8**). Plotting the probability of cavitation as a

18   function of p- (**Fig.6C**) and $p+$ (**Fig.7C**) for control phantoms without nanodroplets demonstrated

19   that the cavitation threshold was not reached even when the frequency compounding transducer was

20   driven at its maximum output pressure for the positive-polarity pulses (p-/$p+$=18.4/61.1 MPa). This

21   finding matched previous work studying the histotripsy intrinsic threshold which has shown that

22   cavitation is only generated when the p- is raised above the intrinsic threshold (~25-30 MPa) (Lin *et*

23   *al.*, 2014a; Lin *et al.*, 2014b; Maxwell *et al.*, 2013; Vlaisavljevich *et al.*, 2015c).

1   For PFH phantoms exposed to the positive-polarity pulses, cavitation was observed once a

2   certain pressure threshold was exceeded (**Fig.8**). However, cavitation did not occur at the geometric

3   focus of the transducer. Instead, the location of the cavitation was ~0.5 mm from the geometric

4   focus, closely matching the location in the field with the highest p- (**Fig.3**). As the pressure was

5   further increased above the NMH cavitation threshold, two separate regions containing cavitation

6   were observed in the PFH phantoms (**Fig.7**), with these locations closely corresponding to the two

7   regions of highest p- as measured by the FOPH (**Fig.3**). The probability of cavitation for PFH

8   phantoms exposed to positive-polarity pulses was plotted as a function of p- (measured at the

9   location corresponding to the highest p-), with the results demonstrating $p_t(-) = 11.4\pm0.1$ MPa, with

10    $\sigma_{mean} = 0.1$ MPa (**Fig.5D**). This p- threshold closely matched the p- threshold for the negative-

11   polarity pulses as well as the p- thresholds previously measured using dual-polarity pulses (**Table

12   1**). Plotting the probability of cavitation for PFH phantoms exposed to positive-polarity pulses as a

13   function of $p+$ resulted in a $p+$ threshold of $p_t(+) = 42.6\pm0.2$ MPa, with $\sigma_{mean} = 0.4$ MPa (**Fig.6D**).

14   This $p+$ threshold was significantly different than the $p+$ thresholds measured for the negative-

15   polarity pulses as well as the $p+$ thresholds previously measured for dual-polarity pulses (**Table 1**).

16   **Figure 9** shows a comparison of the p- and $p+$ thresholds measured for PFH phantoms exposed to

17   the positive-polarity and negative polarity pulses generated in this study as well as dual-polarity

18   pulses at various frequencies (345 kHz–3MHz) measured in a previous study (Vlaisavljevich *et al.*,

19   2015a), with results strongly suggesting that the NMH threshold is a function of the applied p-.

20

Classical Nucleation Theory Simulation

22   A theoretical analysis was performed based on classical nucleation theory (CNT) in order to

23   theoretically investigate the expected cavitation thresholds for phantoms with and without PFH

24   nanodroplets. **Figure 10** shows p_{CNT} compared with the average $p_t(-)$ measured for the near

1   monopolar pulses used in this study as well as for dual polarity pulses at frequencies ranging from

2   345 kHz to 3 MHz used in previous studies (Vlaisavljevich *et al.*, 2015c; Vlaisavljevich *et al.*,

3   2015b). The CNT results predicted a significant decrease in the cavitation threshold for phantoms

4   containing PFH nanodroplets, with the results closely matching the thresholds measured

5   experimentally (**Fig.10**). For example, the predicted *p*- cavitation threshold for PFH phantoms

6   exposed to the negative-polarity pulses used in this study was calculated to be p_{CNT_PFH} = 12.4 MPa,

7   which was close to the experimental measured threshold of $p_t(-) = 11.7\pm0.2$ MPa. The CNT results

8   also predicted a slight increase (~1-3 MPa) in p_{CNT} with increasing frequency, once again matching

9   the trends observed experimentally (**Fig.10**). This slight increase in threshold at higher frequency is

10 due to the smaller focal zone and shorter duration of the applied *p*-. In fact, since bubbles are

11 generated directly from the single *p*- phase of the incident wave, the results of this study suggest

12 that it is more appropriate to use the duration of the applied *p*- as a metric to predict the probability

13 of generating cavitation from these single cycle pulses. The only significant deviation between the

14 experimental and CNT results was observed for phantoms without nanodroplets exposed to the

15 negative-polarity pulses, with the experimental results measuring a threshold ~3.5 MPa greater than

16 predicted by CNT. This difference is likely explained by inaccuracies in the reported pressure

17 values for high pressures (*p*->21.5), which were estimated using a linear summation of individual

18 elements as described in the Methods.

19

Discussion

21   In this work, we were able to generate pulses with dominant negative and positive pressure

22 phases, which allowed us to investigate the effects of positive and negative pressure on the NMH

23 cavitation threshold separately. The results supported our hypothesis that NMH bubbles are

24 generated after cavitation is nucleated inside the droplets directly from the incident *p*- (tensile

1   portion of the incident wave), similar to histotripsy bubbles generated without nanodroplets when

2   the *p-* directly exceeds the intrinsic threshold of the target media. Results showed close agreement

3   in the *p-* threshold for PFH phantoms exposed to negative-polarity (11.4±0.1 MPa), positive-

4   polarity (11.7±0.2 MPa), and dual-polarity (10-15 MPa) pulses. The *p+* thresholds, in contrast, were

5   measured to be significantly different for PFH phantoms exposed to negative-polarity (4.0±0.1

6   MPa), positive-polarity (42.6±0.2 MPa), and dual-polarity (10–16 MPa) pulses. These results

7   support our hypothesis that NMH cavitation is purely dependent upon the applied *p-*. This

8   hypothesis was further supported by the observation that exposing PFH phantoms to positive-

9   polarity pulses resulted in cavitation only being generated in the regions with the highest *p-* (**Fig.8**),

10 as measured by the FOPH (**Fig.3**).

11   The results of this study provide significant insight into the nanodroplet nucleation process

12 and support the hypothesis that the nucleation in NMH can be explained by classical nucleation

13 theory (CNT). The ADV literature has hypothesized that droplet nucleation in ADV is caused by a

14 different mechanism than what is predicted by classical nucleation theory (CNT), based on previous

15 studies showing that the ADV threshold decreases with increasing frequency (Kripfgans *et al.*,

16 2004; Kripfgans *et al.*, 2000; Schad and Hynynen, 2010; Sheeran and Dayton, 2012; Williams *et al.*,

17 2013). Many alternative mechanisms have been proposed to explain the discrepancy between the

18 trends predicted by CNT and the experimental trends observed for ADV including droplet

19 deformation, hydrodynamic cavitation, or acoustic heating (Kripfgans *et al.*, 2004; Kripfgans *et al.*,

20 2000; Sheeran and Dayton, 2012). The results of this study, however, suggest that the nucleation

21 process involved in NMH does in fact follow the mechanism described by CNT, which predicts that

22 cavitation is nucleated inside the droplets directly from the applied *p-*. These results suggest that

23 nanodroplets reduce the cavitation threshold by carrying a lower threshold medium, with the

24 probability of nucleation being a function of the *p-* exposed to the PFC. We think this theory can

1   also be extended to explain the nucleation mechanism for ADV using multi-cycle pulses and

2   various droplet sizes, as recent work has revealed that the decrease in the ADV threshold at higher

3   frequencies is due to superharmonic focusing, which significantly increases the amplitude of the *p-*

4   inside the droplet and is enhanced at higher frequencies and in larger droplets (Li *et al.*, 2014;

5   Shpak *et al.*, 2014). It is likely that the probability of nucleation in ADV will still follow the trends

6   predicted by CNT once the pressure focusing effects are accounted for.

7   Although the results of this work and previous ADV studies suggest that the same

8   nucleation process may be responsible in ADV and NMH, it is important to note that the resulting

9   bubble dynamics are significantly different in these two cases. For example, stable bubbles are

10   formed in ADV (Kripfgans *et al.*, 2004; Kripfgans *et al.*, 2000; Reznik *et al.*, 2013; Reznik *et al.*,

11   2011; Doinikov *et al.*, 2014; Rapoport *et al.*, 2011; Shpak *et al.*, 2013) while NMH produces

12   cavitation bubbles that rapidly expand and then violently collapse (Kim *et al.*, 2013; Vlaisavljevich

13   *et al.*, 2015b; Vlaisavljevich *et al.*, 2013a; Yuksel Durmaz *et al.*, 2014). There are many factors

14   determining the resulting bubble behavior after nucleation, including the ultrasound pulse

15   parameters, initial droplet characteristics, and the properties of the surrounding microenvironment.

16   For example, the higher frequencies and multi-cycle pulses commonly used in ADV result in

17   oscillatory bubble growth, which allows ADV bubbles to stabilize (Reznik *et al.*, 2013; Doinikov *et*

18   *al.*, 2014). In contrast, NMH bubbles are exposed to a single large *p-* at lower frequencies,

19   producing bubbles that rapidly expand to sizes much larger (R_{max}~10-150 μm) than those observed

20   for nanodroplet ADV (R_{max}~1-10 μm), followed by the violent collapse of the NMH bubbles

21   (Reznik *et al.*, 2013; Vlaisavljevich *et al.*, 2015b; Vlaisavljevich *et al.*, 2013a; Yuksel Durmaz *et*

22   *al.*, 2014). In addition to the effects of ultrasound parameters, the resulting bubble behavior is

23   dependent upon the droplet properties (i.e. size, concentration, and PFC boiling point) (Reznik *et*

24   *al.*, 2013; Reznik *et al.*, 2011; Doinikov *et al.*, 2014). Finally, the bubble behavior will also be

highly dependent upon the properties of the surrounding media including the temperature, Young's modulus, viscosity, surface tension, and gas concentration (Doinikov *et al.*, 2014; Reznik *et al.*, 2013; Reznik *et al.*, 2011; Vlaisavljevich *et al.*, 2015b; Vlaisavljevich *et al.*, 2013a; Vlaisavljevich *et al.*, 2015d). It is therefore important to understand the impact of these properties on the resulting bubble dynamics of ADV or NMH therapies, even though the underlying nucleation process is likely the same for these two approaches.

The finding that the nanodroplet nucleation thresholds are determined by the applied *p-* and exhibit a distinct threshold behavior is promising for the development of NMH. This distinct *p-* threshold is dependent upon the droplet properties and can be changed by modulating droplet composition (i.e. changing droplet surface tension to modulate the nucleation threshold) (Vlaisavljevich *et al.*, 2015a). With knowledge of the applied pressure fields and droplet characteristics (i.e. size, composition, concentration), predictable and reliable NMH therapy strategies can be developed. For example, the applied *p-* in NMH therapy must be chosen in the region above the NMH threshold but below the histotripsy intrinsic threshold to ensure cavitation is only generated in regions containing nanodroplets. This approach also suggests that NMH therapy will share the same advantages of histotripsy treatments performed above the intrinsic threshold, such as the generation of precise lesions matching the portion of the beam profile above the *p-* threshold as well as the ability to manipulate bubble dynamics by changing the pulse parameters (Lin *et al.*, 2014b; Maxwell *et al.*, 2013; Vlaisavljevich *et al.*, 2015c; Vlaisavljevich *et al.*, 2015d). Furthermore, the sharp *p-* threshold behavior observed in this study suggests that generating cavitation from nanodroplets is more predictable and reproducible than generating cavitation from micron-sized air contrast agents, which do not require nucleation (i.e. phase transition) in order to initiate the cavitation process and therefore do not show the same distinct threshold behavior (Holland and Apfel, 1990; Miller and Thomas, 1995; Vlaisavljevich *et al.*, 2015c). Overall, the

results of this study improve our understanding of the physical mechanisms underlying the nanodroplet nucleation process, which will help to guide the development of NMH therapy.

Conclusion

In this work, the effects of positive and negative pressure on the NMH cavitation threshold were investigated separately, with results supporting our hypothesis that the NMH cavitation threshold is determined by the incident $p\text{-}$. Close agreement was observed for the $p\text{-}$ thresholds measured for PFH tissue phantoms exposed to negative-polarity (11.4±0.1 MPa) and positive-polarity (11.7±0.2 MPa) pulses. The $p+$ thresholds, in contrast, were significantly different for the negative-polarity (4.0±0.1 MPa) and positive-polarity (42.6±0.2 MPa) pulses. Furthermore, the positive-polarity pulse experiments demonstrated that cavitation was preferentially generated in the regions with the largest $p\text{-}$. In the final part of this study, the experimental results were compared to the cavitation thresholds predicted by classical nucleation theory (CNT), with results showing close agreement between simulations and experiments. Overall, the results of this study support our hypothesis that nanodroplet nucleation is determined by the applied $p\text{-}$ and provide significant insight into the physical mechanisms underlying the NMH process.

Acknowledgements

1   Zhen Xu, Brian Fowlkes, and Kuang-Wei Lin have financial interests and/or other relationship with

2   HistoSonics Inc.
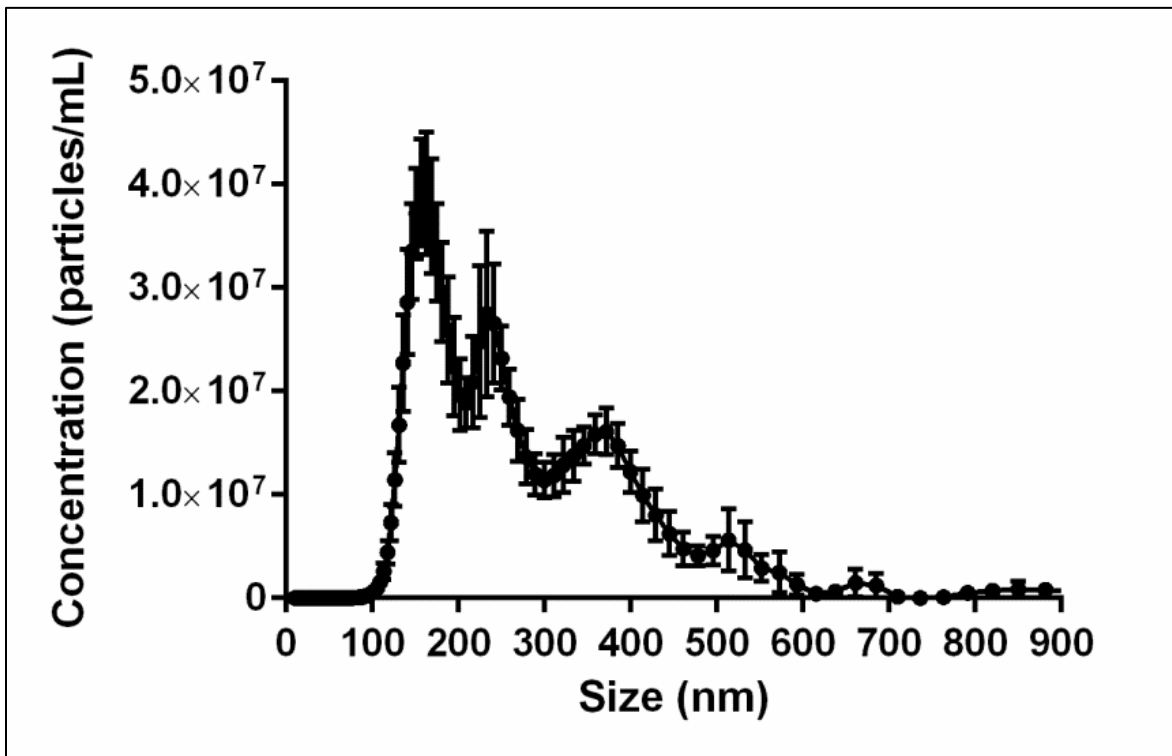
Figures

Figure 1. Nanodroplet characterization. Nanoparticle Tracking Analysis demonstrated PFH nanodroplets had an average size of 233.9±3.9 nm.
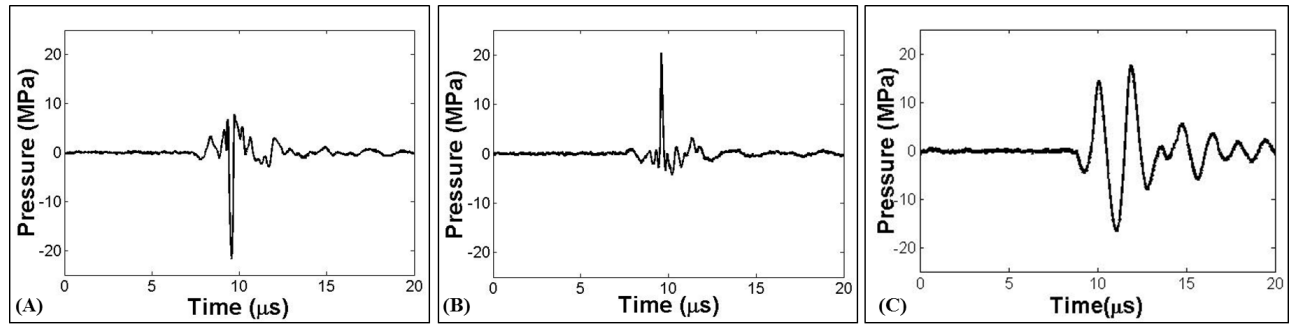
Figure 2. Acoustic waveforms. Example of **(A)** negative-polarity and **(B)** positive-polarity pulses produced by the frequency compounding transducer compared with a **(C)** dual-polarity pulse (500 kHz) previously used in NMH therapy.
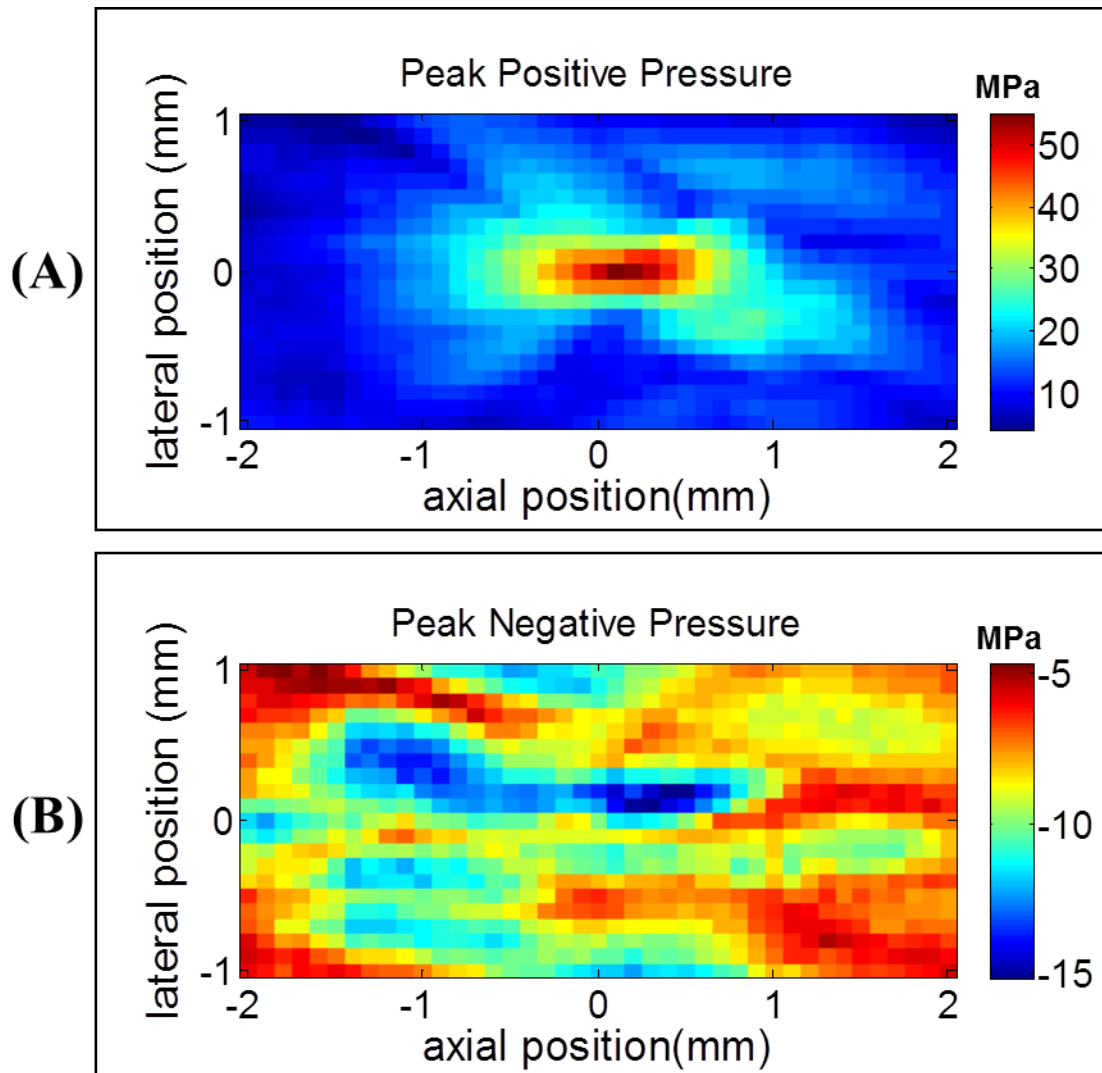
Figure 3. Positive-polarity Pulse: Pressure Fields. 2D spatial pressure fields were measured by the FOPH for a positive-polarity pulse. (**A**) Results demonstrated the location corresponding to the highest positive pressure was near the geometric focus. (**B**) The location corresponding to the highest negative pressure was ~0.5 mm away from the geometric focus in the axial direction.
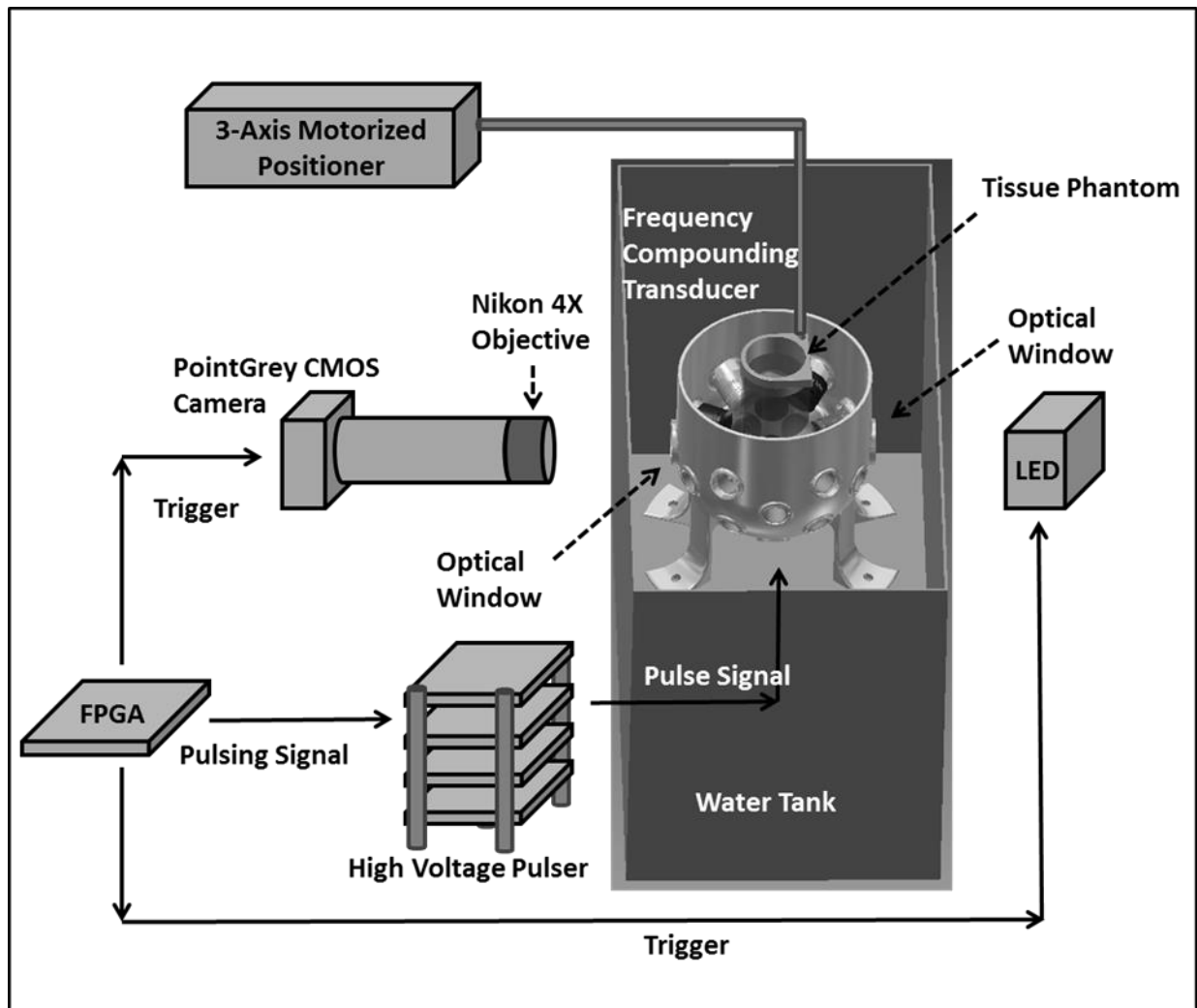
Figure 4. Experimental set-up. Tissue phantoms with and without PFH nanodroplets were placed at the focus of the frequency-compounding transducer (Lin *et al.*, 2014a) for cavitation threshold experiments. Cavitation was monitored using high-speed optical imaging through the transducer's optical windows.

Figure 5. Bubble Images: Negative-polarity Pulses. Optical Images of cavitation bubbles generated from negative-polarity pulses inside (**A**) control phantoms and (**B**) PFH phantoms.
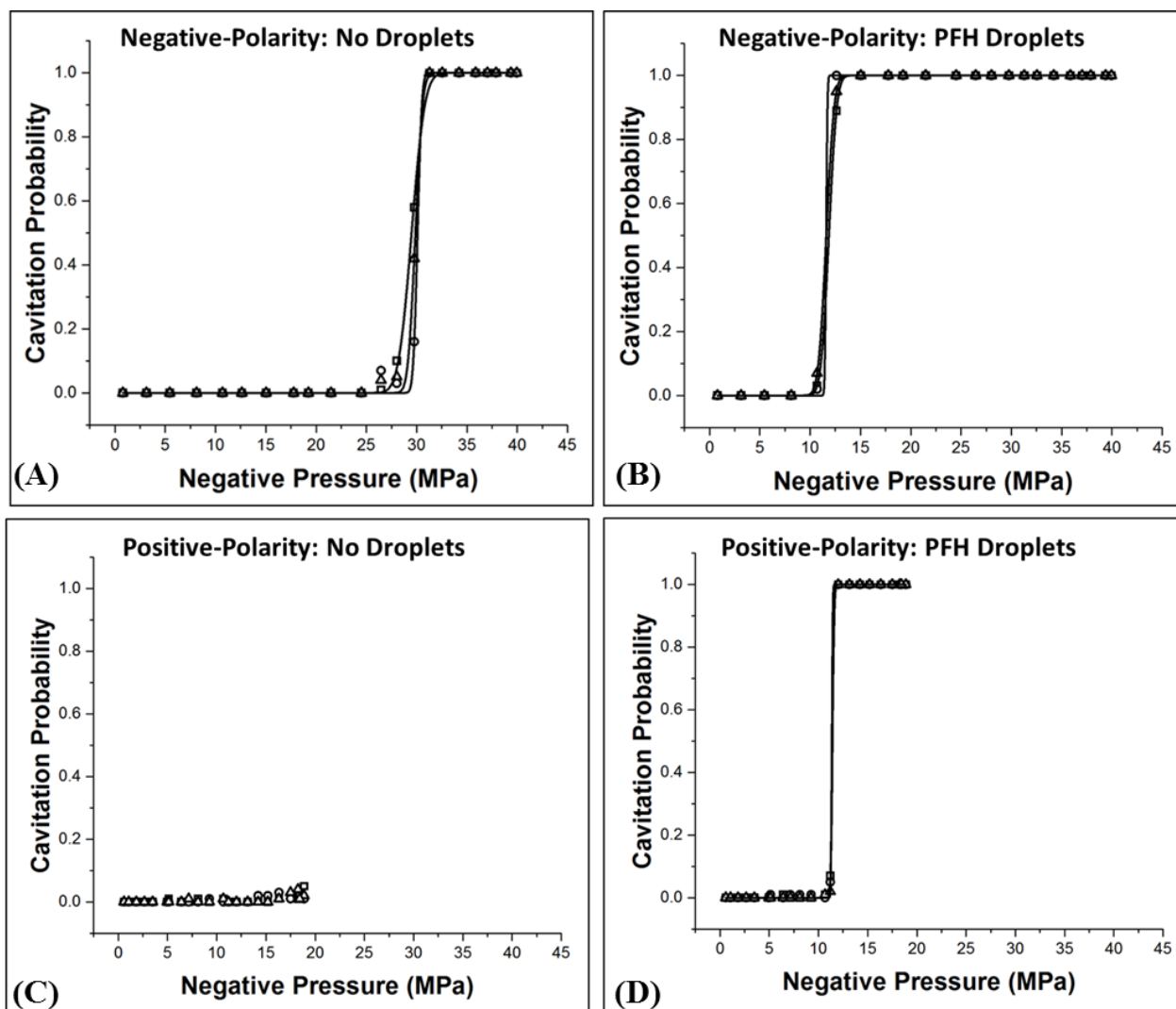
Figure 6. Cavitation Probability vs. Negative Pressure. Plots show the cavitation probability as a function of negative pressure for (**A,C**) control and (**B,D**) PFH phantoms exposed to (**A,B**) negative-polarity pulses and (**C,D**) positive-polarity pulses. The *p-* threshold measured for the negative-polarity and positive-polarity pulses showed close agreement for PFH phantoms. Cavitation couldn't be generated in control phantoms exposed to positive-polarity pulses (Max *p-* =18.4 MPa).

Sample	Pulse Characteristics	P- Threshold (MPa)	P+ Threshold (MPa)
No Droplets	*Dual-Polarity: 345 kHz*	24.8±1.1	31.4±1.5
	Dual-Polarity: 500 kHz	25.5±1.7	28.1±1.9
	Dual-Polarity: 1.5 MHz	26.7±0.4	51.2±2.3
	Dual-Polarity: 3 MHz	26.8±0.5	29.4±29.4
	Negative-Polarity	29.8±0.3	9.9±0.1
	Positive-Polarity	>18.4	>61.1
		P- Threshold (MPa)	**P+ Threshold (MPa)**
PFH Droplets	*Dual-Polarity: 345 kHz*	10.4±0.3	10.2±0.2
	Dual-Polarity: 500 kHz	10.5±0.2	10.7±0.2
	Dual-Polarity: 1.5 MHz	13.0±0.1	14.1±0.2
	Dual-Polarity: 3 MHz	14.9±0.4	15.8±0.4
	Negative-Polarity	11.7±0.2	4.0±0.1
	Positive-Polarity	11.4±0.1	42.6±0.2

Table 1. Threshold Results Comparison. Table shows the values for the *p-* and *p+* thresholds measured for control and PFH phantoms exposed to the negative-polarity and positive-polarity pulses generated by the frequency compounding transducer along with the thresholds previously measured using dual-polarity pulses at 345 kHz, 500 kHz, 1.5 MHz, and 3 MHz (Vlaisavljevich *et al.*, 2015a; Vlaisavljevich *et al.*, 2015b; Vlaisavljevich *et al.*, 2015c). Note: *Italics* represents data taken from previous studies.
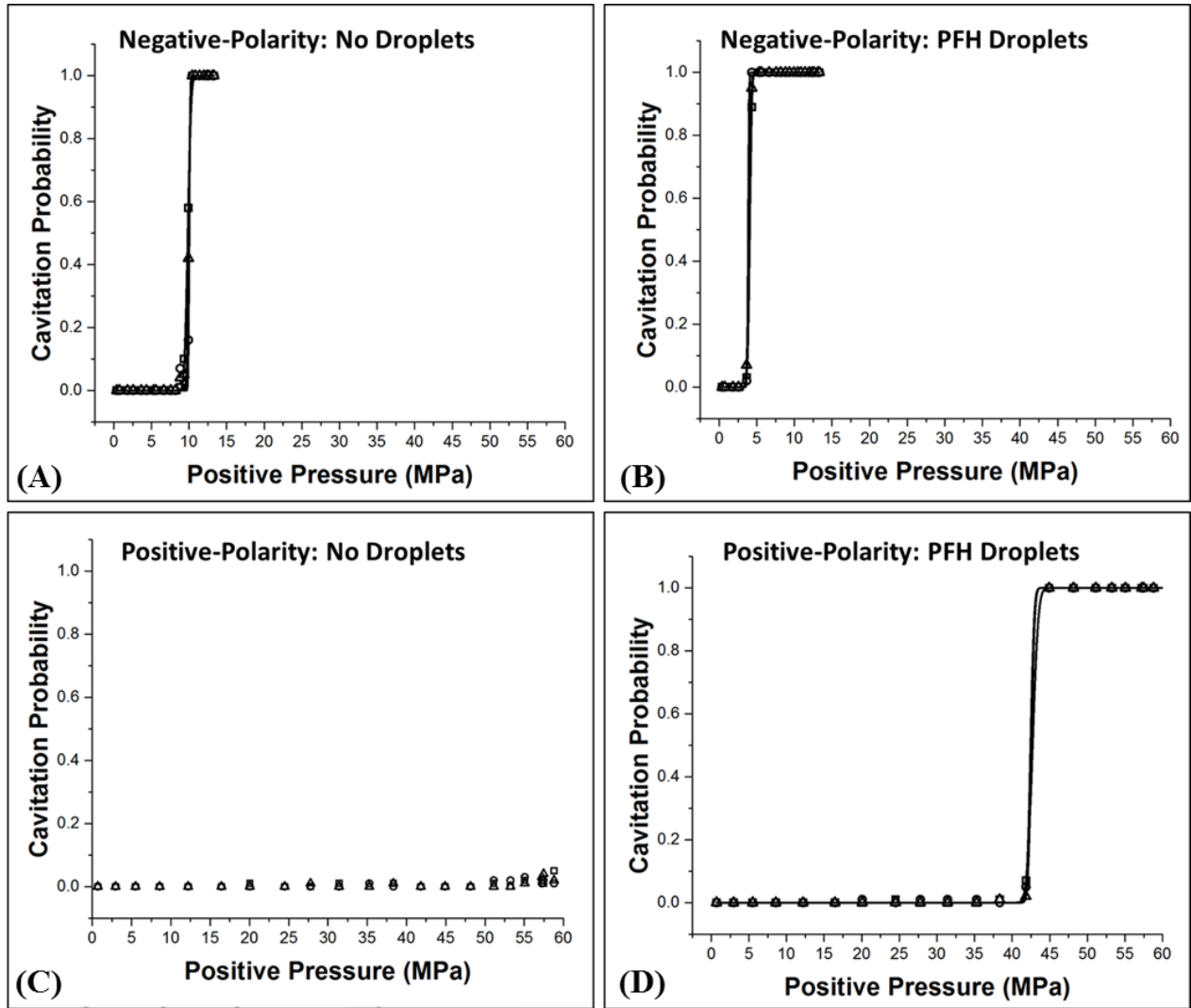
Figure 7. Cavitation Probability vs. Positive Pressure. Plots show the cavitation probability as a function of positive pressure for (**A,C**) control and (**B,D**) PFH phantoms exposed to (**A,B**) negative-polarity pulses and (**C,D**) positive-polarity pulses. A significant increase in the $p+$ threshold was observed for both control and PFH phantoms exposed to the positive-positive polarity pulses.
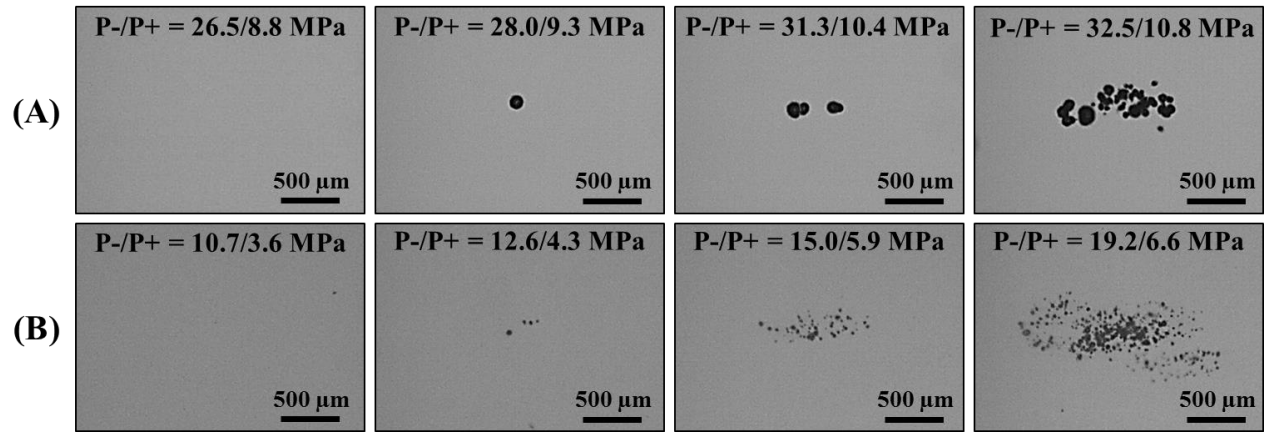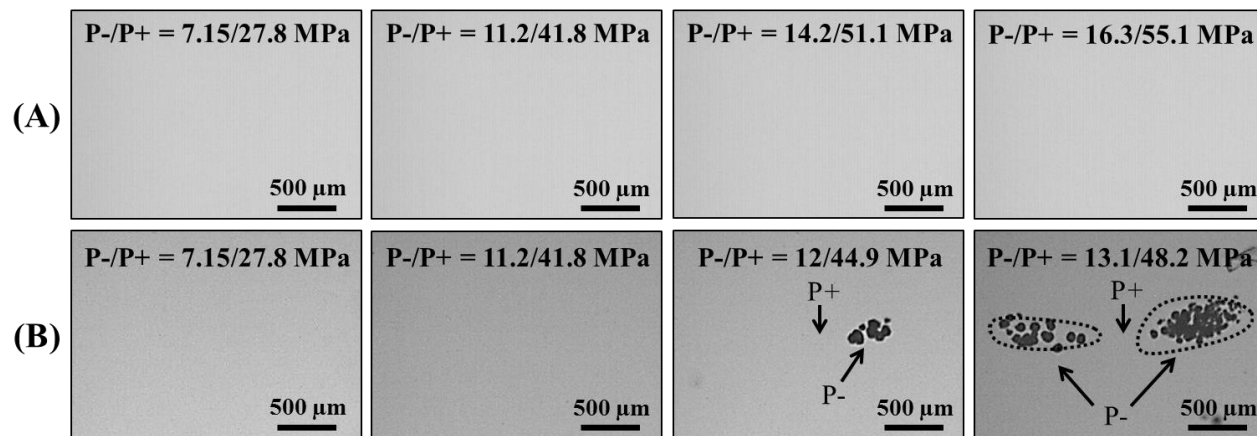
Figure 8. Bubble Images: Positive-polarity Pulses. Optical Images of cavitation bubbles generated from positive-polarity pulses inside (**A**) control phantoms and (**B**) PFH phantoms. Arrows on the plot indicate the locations in the focal region corresponding to the highest positive ($p+$) and negative ($p-$) pressures as measured by the FOPH (**Fig.3**). Dashed lines correspond to the approximate regions with a $p-$ above ~12 MPa (**Fig.3**).
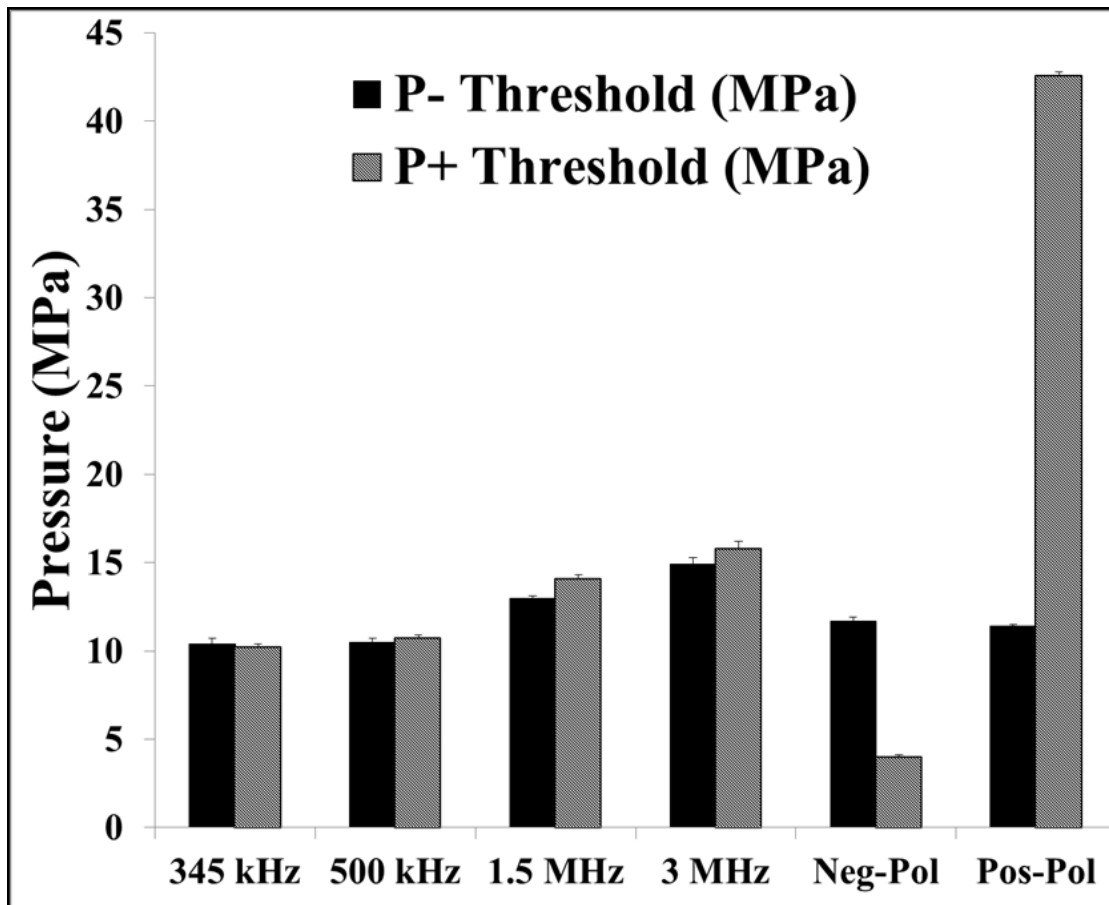
Figure 9. NMH Threshold Results Comparison. Plot compares the *p-* and *p+* thresholds measured for PFH phantoms in this study (negative-polarity and positive-polarity pulses) with the thresholds previously measured using dual-polarity pulses (f=345kHz, 500kHz, 1.5MHz, 3 MHz) (Vlaisavljevich *et al.*, 2015a). Results suggest NMH cavitation is generated directly from the *p-* of the incident wave.
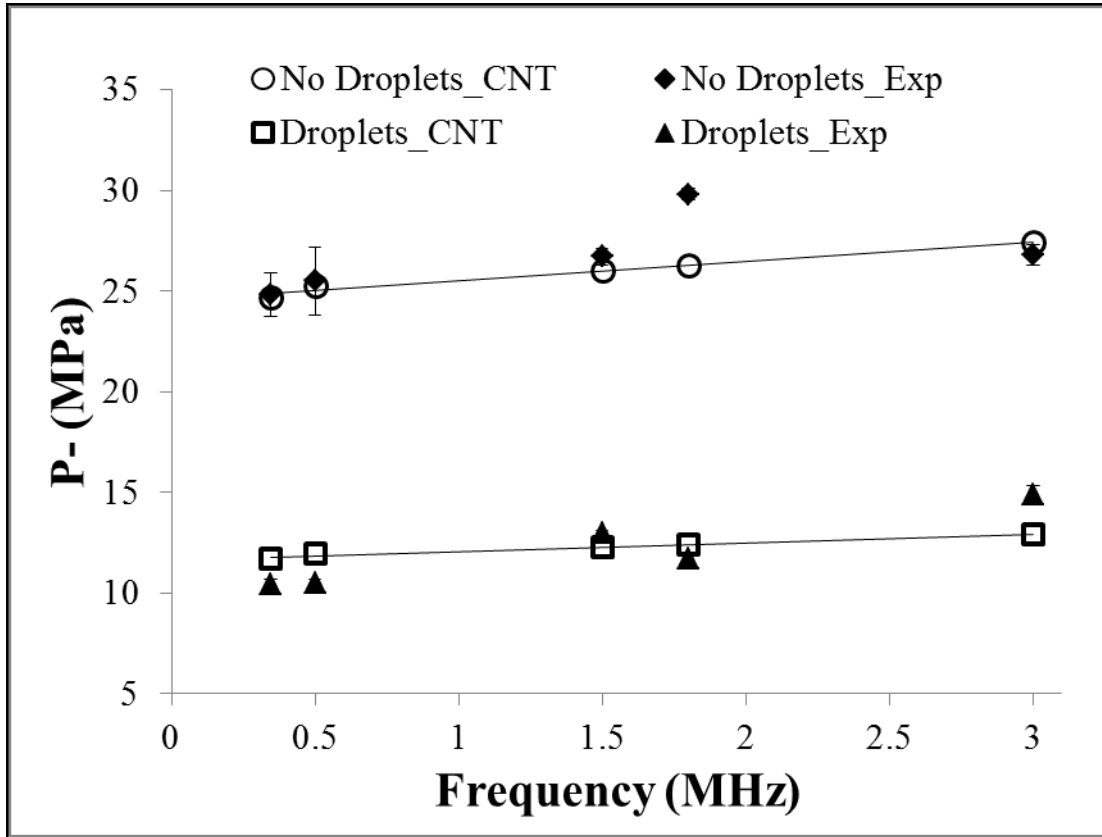
Figure 10. CNT Simulation. Classical nucleation theory was used to predict the cavitation thresholds for histotripsy pulses applied to phantoms with and without PFH nanodroplets. Results showed close agreement between the CNT simulation and the experimentally measured thresholds. Note that the waveforms produced by the frequency compounding transducer are plotted as an effective frequency of 1.8 MPa.

References

Arvengas A, Davitt K and Caupin F 2011 Fiber optic probe hydrophone for the study of acoustic cavitation in water *Rev Sci Instrum* **82** 034904

Caupin F and Herbert E 2006 Cavitation in water: a review *Comptes Rendus Physique* **7** 1000-17

Doinikov A A, Sheeran P S, Bouakaz A and Dayton P A 2014 Vaporization dynamics of volatile perfluorocarbon droplets: a theoretical model and in vitro validation *Med Phys* **41** 102901

Fisher J C 1948 The Fracture of Liquids *Journal of Applied Physics* **19** 1062-7

Hempel C R, Hall T L, Cain C A, Fowlkes J B, Xu Z and Roberts W W 2011 Histotripsy fractionation of prostate tissue: local effects and systemic response in a canine model *J Urol* **185** 1484-9

Herbert E, Balibar S and Caupin F 2006 Cavitation pressure in water *Phys Rev E Stat Nonlin Soft Matter Phys* **74** 041603

Holland C K and Apfel R E 1990 Thresholds for transient cavitation produced by pulsed ultrasound in a controlled nuclei environment *J Acoust Soc Am* **88** 2059-69

Hosmer D W and Lemeshow S 1992 Confidence interval estimation of interaction *Epidemiology* **3** 452-6

Hougham G, Cassidy P E, K. J and Davidson T 1999 *Fluoropolymers 2: Properties*: Kluwer Academic Publishers

Kawabata K, Asami R, Axuma T and Umemura S 2010 Acoustic response of microbubbles derived from phase-change nanodroplet. *Jpn J Appl Phys*

Kim Y, Gelehrter S K, Fifer C G, Lu J C, Owens G E, Berman D R, Williams J, Wilkinson J E, Ives K A and Xu Z 2011 Non-invasive pulsed cavitational ultrasound for fetal tissue ablation: feasibility study in a fetal sheep model *Ultrasound in Obstetrics & Gynecology* **37** 450-7

Kim Y H, Fifer C G, Gelehrter S K, Owens G E, Berman D R, Vlaisavljevich E, Allen S P, Ladino-Torres M F and Xu Z 2013 Developmental Impact and Lesion Maturation of Histotripsy-Mediated Non-Invasive Tissue Ablation in a Fetal Sheep Model *Ultrasound in Medicine and Biology* **39** 1047-55

Kripfgans O D, Fabiilli M L, Carson P L and Fowlkes J B 2004 On the acoustic vaporization of micrometer-sized droplets *J Acoust Soc Am* **116** 272-81

Kripfgans O D, Fowlkes J B, Miller D L, Eldevik O P and Carson P L 2000 Acoustic droplet vaporization for therapeutic and diagnostic applications *Ultrasound Med Biol* **26** 1177-89

Li D S, Kripfgans O D, Fabiilli M L, Brian Fowlkes J and Bull J L 2014 Initial nucleation site formation due to acoustic droplet vaporization *Appl Phys Lett* **104** 063703

Lin K W, Hall T L, McGough R J, Xu Z and Cain C A 2014a Synthesis of monopolar ultrasound pulses for therapy: the frequency-compounding transducer *IEEE Trans Ultrason Ferroelectr Freq Control* **61** 1123-36

Lin K W, Kim Y, Maxwell A D, Wang T Y, Hall T L, Xu Z, Fowlkes J B and Cain C A 2014b Histotripsy beyond the intrinsic cavitation threshold using very short ultrasound pulses: microtripsy *IEEE Trans Ultrason Ferroelectr Freq Control* **61** 251-65

Maxwell A D, Cain C A, Hall T L, Fowlkes J B and Xu Z 2013 Probability of cavitation for single ultrasound pulses applied to tissues and tissue-mimicking materials *Ultrasound Med Biol* **39** 449-65

Maxwell A D, Owens G, Gurm H S, Ives K, Myers D D, Jr. and Xu Z 2011 Noninvasive treatment of deep venous thrombosis using pulsed ultrasound cavitation therapy (histotripsy) in a porcine model *J Vasc Interv Radiol* **22** 369-77

Miller D L and Thomas R M 1995 Ultrasound contrast agents nucleate inertial cavitation in vitro *Ultrasound Med Biol* **21** 1059-65

Owens G E, Miller R M, Ensing G, Ives K, Gordon D, Ludomirsky A and Xu Z 2011 Therapeutic ultrasound to noninvasively create intracardiac communications in an intact animal model *Catheter Cardiovasc Interv* **77** 580-8

Parsons J E, Cain C A, Abrams G D and Fowlkes J B 2006a Pulsed cavitational ultrasound therapy for controlled tissue homogenization *Ultrasound Med Biol* **32** 115-29

Parsons J E, Cain C A and Fowlkes J B 2006b Cost-effective assembly of a basic fiber-optic hydrophone for measurement of high-amplitude therapeutic ultrasound fields *J Acoust Soc Am* **119** 1432-40

Pettersen M S, Balibar S and Maris H J 1994 Experimental investigation of cavitation in superfluid 4He *Phys Rev B Condens Matter* **49** 12062-70

Rapoport N, Nam K-H, Gupta R, Gao Z, Mohan P, Payne A, Todd N, Liu X, Kim T, Shea J, Scaife C, Parker D L, Jeong E-K and Kennedy A M 2011 Ultrasound-mediated tumor imaging and nanotherapy using drug loaded, block copolymer stabilized perfluorocarbon nanoemulsions *Journal of Controlled Release* **153** 4-15

Reznik N, Shpak O, Gelderblom E C, Williams R, de Jong N, Versluis M and Burns P N 2013 The efficiency and stability of bubble formation by acoustic vaporization of submicron perfluorocarbon droplets *Ultrasonics* **53** 1368-76

Reznik N, Williams R and Burns P N 2011 Investigation of Vaporized Submicron Perfluorocarbon Droplets as an Ultrasound Contrast Agent *Ultrasound in Medicine and Biology* **37** 1271-9

Roberts W W, Hall T L, Ives K, Wolf J S, Jr., Fowlkes J B and Cain C A 2006 Pulsed cavitational ultrasound: a noninvasive technology for controlled tissue ablation (histotripsy) in the rabbit kidney *J Urol* **175** 734-8

Schad K C and Hynynen K 2010 In vitro characterization of perfluorocarbon droplets for focused ultrasound therapy *Phys Med Biol* **55** 4933-47

Sheeran P S and Dayton P A 2012 Phase-change contrast agents for imaging and therapy *Curr Pharm Des* **18** 2152-65

Shpak O, Kokhuis T J, Luan Y, Lohse D, de Jong N, Fowlkes B, Fabiilli M and Versluis M 2013 Ultrafast dynamics of the acoustic vaporization of phase-change microdroplets *J Acoust Soc Am* **134** 1610-21

Shpak O, Verweij M, Vos H J, de Jong N, Lohse D and Versluis M 2014 Acoustic droplet vaporization is initiated by superharmonic focusing *Proc Natl Acad Sci U S A* **111** 1697-702

Styn N R, Wheat J C, Hall T L and Roberts W W 2010 Histotripsy of VX-2 tumor implanted in a renal rabbit model *J Endourol* **24** 1145-50

Vlaisavljevich E, Aydin O, Lin K W, Fowlkes J B, ElSayed M and Xu Z 2015a Investigation of the Role of Ultrasound Frequency and Droplet Composition in Nanodroplet-mediated Histotripsy. In: *International Society for Therapeutic Ultrasound,* (Utrecht, Netherlands

Vlaisavljevich E, Aydin O, Yuksel Durmaz Y, Lin K W, Fowlkes B, ElSayed M and Xu Z 2015b Effects of Ultrasound Frequency on Nanodroplet-Mediated Histotripsy *Ultrasound Med Biol* **41** 2135-47

Vlaisavljevich E, Durmaz Y Y, Maxwell A, Elsayed M and Xu Z 2013a Nanodroplet-mediated histotripsy for image-guided targeted ultrasound cell ablation *Theranostics* **3** 851-64

Vlaisavljevich E, Kim Y, Allen S, Owens G, Pelletier S, Cain C, Ives K and Xu Z 2013b Image-Guided Non-Invasive Ultrasound Liver Ablation using Histotripsy: Feasibility Study in an *In Vivo* Porcine Model. *Ultrasound Med Biol*

Vlaisavljevich E, Lin K W, Maxwell A, Warnez M, Mancia L, Singh R, Putnam A, fowlkes J B, Johnsen E, Cain C and Xu Z 2015c Effects of Ultrasound Frequency and Tissue Stiffness on the Histotripsy Intrinsic Threshold for Cavitation *Ultrasound Med Biol*

Vlaisavljevich E, Lin K W, Warnez M, Singh R, Mancia L, Putnam A, Johnsen E, Cain C and Xu Z 2015d Effects of Tissue Stiffness, Ultrasound Frequency, and Pressure on Histotripsy-induced Cavitation Bubble Behavior *Phys Med Biol*

Williams R, Wright C, Cherin E, Reznik N, Lee M, Gorelikov I, Foster F S, Matsuura N and Burns P N 2013 Characterization of submicron phase-change perfluorocarbon droplets for extravascular ultrasound imaging of cancer *Ultrasound Med Biol* **39** 475-89

Xu Z, Fowlkes J B, Rothman E D, Levin A M and Cain C A 2005 Controlled ultrasound tissue erosion: the role of dynamic interaction between insonation and microbubble activity *J Acoust Soc Am* **117** 424-35

Xu Z, Owens G, Gordon D, Cain C and Ludomirsky A 2010 Noninvasive creation of an atrial septal defect by histotripsy in a canine model *Circulation* **121** 742-9

Yuksel Durmaz Y, Vlaisavljevich E, Xu Z and ElSayed M 2014 Development of nanodroplets for histotripsy-mediated cell ablation *Mol Pharm* **11** 3684-95